AGU PUBLICATIONS

Geochemistry, Geophysics, Geosystems

RESEARCH ARTICLE
10.1002/2014GC005411

Special Section:
Magnetism From Atomic to Planetary Scales: Physical Principles and Interdisciplinary Applications in Geo- and Planetary Sciences

Key Points:
- We provide evidence for the presence of biogenic greigite in ancient sediments
- Diagenetic greigite enhancements are climatically controlled
- Greigite is a paleoenvironmental indicator in anoxic environments

Supporting Information:
- Readme
- Figures S1–S7

Correspondence to:
L. Chang,
liao.chang@anu.edu.au

Citation:
Chang, L., I. Vasiliev, C. van Baak, W. Krijgsman, M. J. Dekkers, A. P. Roberts, J. D. Fitz Gerald, A. van Hoesel, and M. Winklhofer (2014), Identification and environmental interpretation of diagenetic and biogenic greigite in sediments: A lesson from the Messinian Black Sea, *Geochem. Geophys. Geosyst.*, *15*, 3612–3627, doi:10.1002/2014GC005411.

Received 9 MAY 2014
Accepted 8 AUG 2014
Accepted article online 16 AUG 2014
Published online 12 SEP 2014

Identification and environmental interpretation of diagenetic and biogenic greigite in sediments: A lesson from the Messinian Black Sea

Liao Chang[1,2], Iuliana Vasiliev[1], Christiaan van Baak[1], Wout Krijgsman[1], Mark J. Dekkers[1], Andrew P. Roberts[2], John D. Fitz Gerald[2], Annelies van Hoesel[3], and Michael Winklhofer[4]

[1]Paleomagnetic Laboratory "Fort Hoofddijk," Department of Earth Sciences, Utrecht University, Utrecht, Netherlands, [2]Research School of Earth Sciences, Australian National University, Canberra, Australian Capital Territory, Australia, [3]Department of Earth Sciences, Utrecht University, Utrecht, Netherlands, [4]Department of Earth and Environmental Sciences, Ludwig-Maximilians University, Munich, Germany

Abstract Greigite (Fe_3S_4) is a widespread authigenic magnetic mineral in anoxic sediments and is also commonly biosynthesized by magnetotactic bacteria in aqueous environments. While the presence of fossilized bacterial magnetite (Fe_3O_4) has now been widely demonstrated, the preservation of greigite magnetofossils in the geological record is only poorly constrained. Here we investigate Mio-Pliocene sediments of the former Black Sea to test whether we can detect greigite magnetofossils and to unravel potential environmental controls on greigite formation. Our magnetic analyses and transmission electron microscope (TEM) observations indicate the presence of both diagenetic and bacterial greigite, and suggest a potentially widespread preservation of greigite magnetofossils in ancient sediments, which has important implications for assessing the reliability of paleomagnetic records carried by greigite. TEM-based chemical and structural analyses also indicate the common presence of nickel-substituted diagenetic iron sulfide crystals with a ferrimagnetic greigite structure. In addition, our cyclostratigraphic framework allows correlation of magnetic properties of Messinian Black Sea sediments (Taman Peninsula, Russia) to global climate records. Diagenetic greigite enhancements appear to be climatically controlled, with greigite mainly occurring in warm/wet periods. Diagenetic greigite formation can be explained by variations in terrigenous inputs and dissolved pore water sulfate concentrations in different sedimentary environments. Our analysis demonstrates the usefulness of greigite for studying long-term climate variability in anoxic environments.

1. Introduction

Greigite (Fe_3S_4) is a widespread iron sulfide mineral that has been found in anoxic sedimentary environments across the world over geologically significant time periods [*Roberts et al*., 2011a]. It is a strongly ferrimagnetic mineral that makes important contributions to paleomagnetic and environmental records. Paleomagnetic records carried by greigite can be challenging to interpret because greigite can form at different periods significantly later than deposition, which then leads to anomalous paleomagnetic records and remagnetization [e.g., *Jiang et al*., 2001; *Roberts and Weaver*, 2005; *Rowan and Roberts*, 2006; *Roberts et al*., 2010; *Sagnotti et al*., 2010]. But greigite can also form during earliest burial and, thus, record an excellent paleomagnetic signal [e.g., *Tric et al*., 1991; *Vasiliev et al*., 2004, 2005; *Hüsing et al*., 2007] that matches well with the geomagnetic polarity time scale (GPTS) [*Cande and Kent*, 1995] and provides crucial age control for sedimentary sequences. Greigite is also useful for paleoenvironmental analysis. For example, greigite abundances from the Santa Barbara Basin have been demonstrated to reflect millennial-scale climate variability [*Blanchet et al*., 2009].

In sulfate-reducing sedimentary environments, greigite often forms as a precursor to pyrite (FeS_2). As an intermediate phase that forms during pyritization, greigite is expected to fully convert to pyrite during early diagenetic sedimentary sulfate reduction [*Berner*, 1984]. *Kao et al*. [2004] demonstrated that when reactive iron is abundant and dissolved sulfide concentrations are low in sedimentary pore waters, pyritization can be arrested and greigite can be preserved, because dissolved sulfide (H_2S, HS^-) is fully consumed by reactive

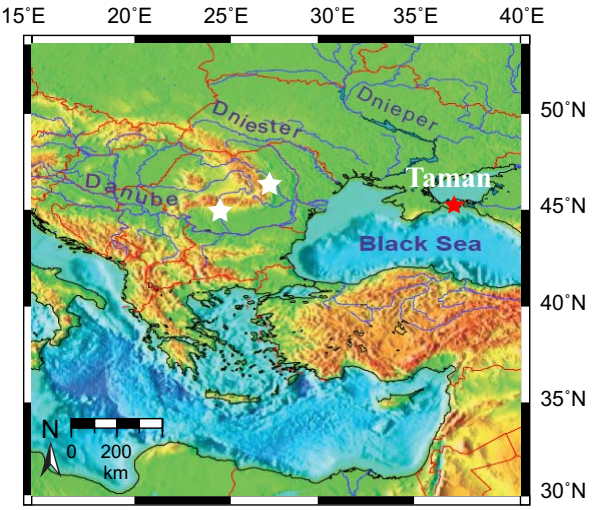

Figure 1. Map of the Black Sea domain of the Paratethys region with locations of the studied sedimentary sections in the Taman Peninsula, Russia (red star) [*Krijgsman et al.*, 2010] and in Romania (white stars) [*Vasiliev et al.*, 2004, 2005], where putative greigite magnetofossils have been reported [*Vasiliev et al.*, 2008].

iron. *Roberts and Weaver* [2005] argued that greigite can grow at any time during diagenesis when iron and sulfide are available. Formation and preservation of diagenetic greigite in sediments can be complex and can preclude straightforward interpretation of magnetic signals carried by greigite.

Greigite is also often produced by sulfidic magnetotactic bacteria (MTB) in natural environments [*Farina et al.*, 1990; *Mann et al.*, 1990]. MTB intracellularly biomineralize chains of greigite or magnetite (Fe_3O_4) crystals as microscopic compasses that enable them to move along geomagnetic field lines to find optimal living conditions [*Bazylinski and Frankel*, 2004]. The inorganic remains of MTB preserved in sediments as magnetofossils can make significant contributions to paleomagnetic signals [e.g., *Kirschvink and Chang*, 1984; *Petersen et al.*, 1986; *Stoltz et al.*, 1986; *Roberts et al.*, 2012; *Heslop et al.*, 2013] and can reflect environmental processes, such as glacial-interglacial fluctuations [*Hesse*, 1994; *Yamazaki*, 2012; *Heslop et al.*, 2013], hyperthermal events [*Kopp et al.*, 2007; *Schumann et al.*, 2008; *Chang et al.*, 2012; *Larrasoaña et al.*, 2012], and oceanic productivity [*Roberts et al.*, 2011b; *Yamazaki and Ikehara*, 2012; *Chang et al.*, 2013].

Unlike diagenetic greigite, which can remagnetize sediments or overprint primary remanences due to post-depositional growth, bacterial greigite should carry a syndepositional paleomagnetic signal that is useful for magnetostratigraphic dating and paleomagnetic reconstructions [*Vasiliev et al.*, 2008]. Compared to magnetite-producing MTB, greigite producers are less common in modern environments, although they have been identified in many sulfide-rich aquatic environments [e.g., *Farina et al.*, 1990; *Mann et al.*, 1990; *Bazylinski et al.*, 1995; *Pósfai et al.*, 1998a, 1998b; *Simmons et al.*, 2004; *Reitner et al.*, 2005; *Wenter et al.*, 2009; *Lefèvre et al.*, 2011; *Wang et al.*, 2013]. Preservation of magnetite magnetofossils in sediments was expected to be common since the discovery of MTB in the 1970s [*Kirschvink and Chang*, 1984; *Petersen et al.*, 1986; *Stoltz et al.*, 1986; *Hesse*, 1994; *Hounslow and Maher*, 1996], and they are now being frequently reported [*Kopp et al.*, 2007; *Kopp and Kirschvink*, 2008; *Roberts et al.*, 2011b, 2012; *Chang et al.*, 2012; *Larrasoaña et al.*, 2012; *Yamazaki*, 2012; *Heslop et al.*, 2013]. In contrast, geological preservation of greigite magnetofossils is not well documented. Putative greigite magnetofossils have been reported from Miocene and Pliocene sediments from the Carpathian foredeep, Romania [*Pósfai et al.*, 2001; *Vasiliev et al.*, 2008]. Bacterial greigite has also been identified within Baltic Sea sapropels up to several thousand years in age [*Reinholdsson et al.*, 2013]. Similar magnetic properties suggest that biogenic greigite may also magnetically dominate some Mediterranean sapropels [*Roberts et al.*, 1999; *Reinholdsson et al.*, 2013]. In order to assess the preservation potential of greigite magnetofossils in the geological record and to study greigite formation under changing environmental and climatic conditions, we use rock magnetic techniques, transmission electron microscope (TEM) observations, X-ray fluorescence (XRF), and cyclostratigraphy, to investigate Mio-Pliocene Black Sea sediments.

2. Geological Setting and Astronomical Tuning

Samples from several Mio-Pliocene sedimentary sections in the former Black Sea basin in Russia and Romania were selected for this study (Figure 1). Samples labeled "TK-XXX" and "TR-XXX" are from the Zheleznyi Rog (Iron Cape) section on the Black Sea margin of the Taman Peninsula, Russia. Standard paleomagnetic drill cores were taken at ~1–2 m stratigraphic intervals. This section is 500 m thick and covers ~5 Myr of Mio-Pliocene sedimentation in the Black Sea domain of the Paratethys Sea [*Vasiliev et al.*, 2011]. We focus

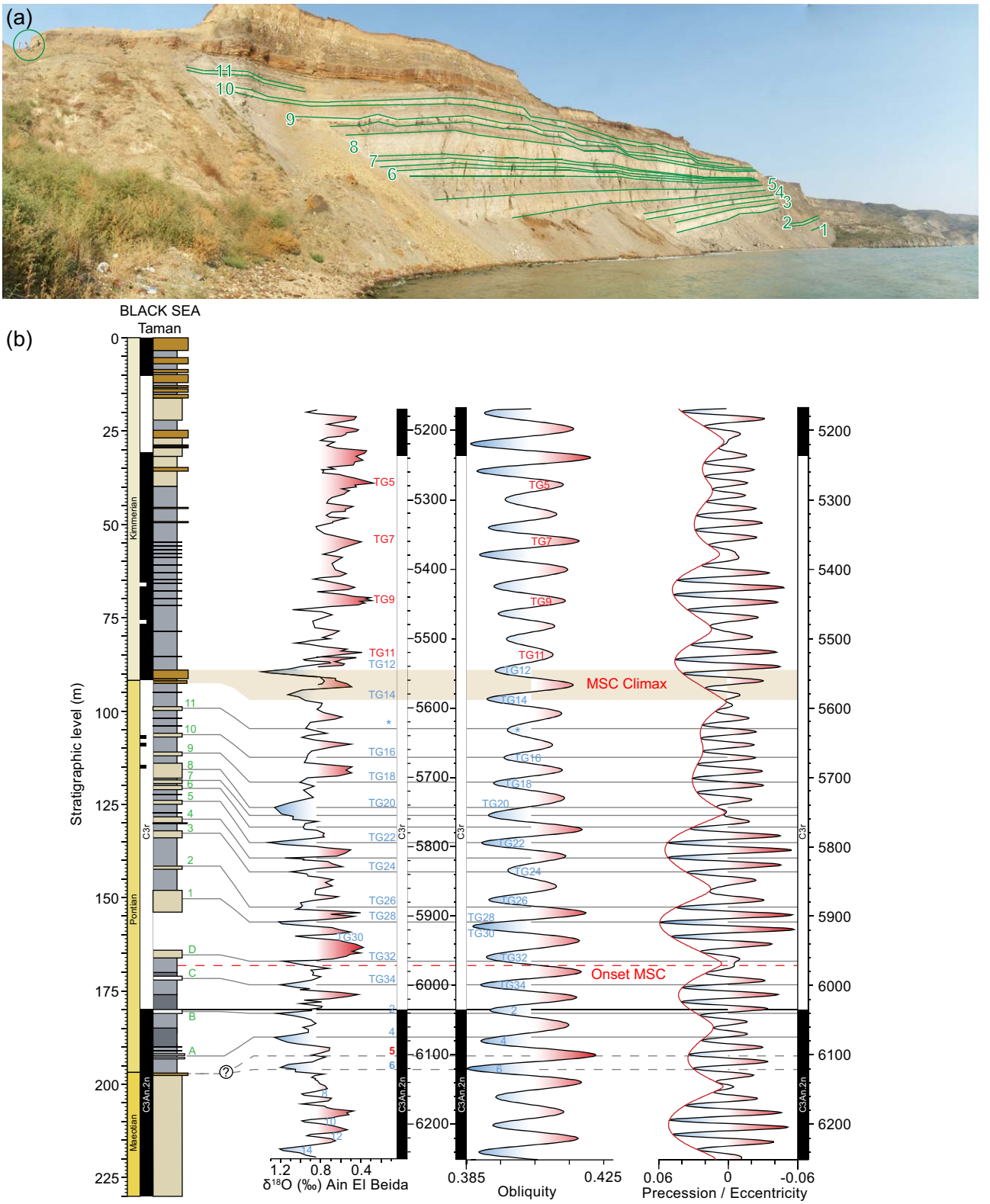

Figure 2. Chronology and climate stratigraphy for the Zheleznyi Rog section on the Black Sea coast, Taman Peninsula, Russia. (a) Field photograph with clear dark-light alternations related to climatic cyclicity. (b) Tentative astronomical tuning of the cyclic sediments to the La2004 astronomical solution [*Laskar et al.*, 2004] and benthic $\delta^{18}O$ records for the upper Miocene Ain el Beida section, northwestern Morocco [*Van der Laan et al.*, 2005, 2006]. Numbers in Figure 2a correlate to the numbers in the lithostratigraphic log in Figure 2b. The green circle in (a) indicates people in the field as a scale.

on the upper 250 m of the section (Pontian and Kimmerian regional stages) [*Krijgsman et al*., 2010]. This is the time equivalent of the Messinian Salinity Crisis (MSC; 5.97–5.33 Ma) [*Manzi et al*., 2013; *Roveri et al*., 2014]. The base of the Pontian is characterized by a marine flooding event, which represents a reconnection of the Black Sea to the Mediterranean Sea [*Krijgsman et al*., 2010]. This event was followed by reestablishment of brackish conditions in the Black Sea basin and a major invasion of Pannonian species [*Stoica et al*., 2013; *Grothe et al*., 2014].

The Pontian sedimentary succession is characterized by distinct dark-light alternations (labeled A–D and 1–11 in Figure 2a), which indicate stable depositional conditions and a potential link to (astronomically) forced climate cyclicity. The alternations pass upward from dark bedded bituminous clay and marl, to diatomite couplets (A–C), to light and dark gray marls (D, 1–11). The diatomite couplets reflect increased marine conditions compared to the interbedded marls and represent diatom blooms at the transition between marine and freshwater conditions [*Radionova and Golovina*, 2011; *Radionova et al*., 2012]. Straightforward correlation to either obliquity or precession cannot be made; correlation to the astronomically tuned δ^{18}O record of *Van der Laan et al*. [2005, 2006] provides a more straightforward pattern fit. This record from the Atlantic site of Morocco is the nearest oxygen isotope record not influenced by MSC evaporites and is taken as representative of regional climate. In our interpretation, light intervals correlate to cold/glacial stages and darker intervals to warmer/interglacial stages. The darker marls may represent a higher terrestrial component, related to higher river discharge during interglacial periods. In glacial periods, this is reduced and the "marine" calcite component is more dominant.

The geomagnetic reversal at 180 m is an age correlation tie-point that corresponds to the C3An.1n-C3r reversal at 6.033 Ma [*Krijgsman et al*., 2010; *Vasiliev et al*., 2011]. Our cyclostratigraphic correlation suggests a flooding age for the base of the Pontian to have been around 6.1 Ma, rather than the previously suggested 6.04 Ma [*Krijgsman et al*., 2010]. The majority of the Pontian was deposited during the long C3r reversed chron, which provides no additional magnetostratigraphic tie-points. The pattern of light beds 3–8 is, however, distinct and appears to correlate well with glacial δ^{18}O stages TG 24 to TG 20 (Figure 2b). Overlying the Pontian marls is a distinct reddish interval that contains oolites/pisolites and nodular marls, which suggest high-energy coastal deposition. This reddish layer marks the base of the Kimmerian stage and is interpreted as the MSC climax related to glacial peaks TG 12 and TG 14, which recorded a sea level drop in the Black Sea basin [*Krijgsman et al*., 2010]. Faunal indicators suggest a change from brackish-marine conditions in the Pontian stages to a freshwater environment in the Kimmerian [*Krijgsman et al*., 2010], where no clear lithological cyclicity is observed.

Selected samples ("BD-XXX" and "RR-XXX") from Pliocene Black Sea sediments of the Romanian Carpathians [*Vasiliev et al*., 2004, 2005] were also analyzed. These sediments, consisting of blue to gray sandstones, siltstones and clays, were deposited at high sedimentation rates (60–150 cm/kyr) in brackish environments. The samples are the same as those studied by *Vasiliev et al*. [2008]. Several synthetic greigite samples ("S-XXX") [*Chang et al*., 2007, 2008] and magnetite magnetofossil-bearing sediment samples were analyzed to compare with results from greigite-bearing sediments. Sample "CD143-1-21" is a surface sediment sample (21 cm below the surface) from piston core CD143–55705 from the Oman margin [*Rowan et al*., 2009]. Sample "738C-11R1–40" is a pelagic carbonate from the Paleocene-Eocene thermal maximum from ODP Hole 738C, Southern Ocean [*Larrasoaña et al*., 2012]. Sample "689D-11H6–21" is an early Oligocene pelagic carbonate from ODP Hole 689D, Southern Ocean [*Roberts et al*., 2012].

3. Methods

Room temperature hysteresis, isothermal remanent magnetization (IRM) acquisition, backfield demagnetization, and FORC measurements were performed using a Princeton Measurements Corporation MicroMag alternating gradient magnetometer (AGM) (Model 2900; noise level 2×10^{-9} Am^2) at the Paleomagnetic Laboratory of Utrecht University. Hysteresis loops were measured between ± 1 T with a field step of 4 mT and a 150 ms averaging time. Hysteresis parameters, including the saturation magnetization (M_s), the saturation remanent magnetization (M_{rs}), and coercivity (B_c), were determined after paramagnetic slope correction. FORC diagrams [*Pike et al*., 1999; *Roberts et al*., 2000] were obtained with maximum applied fields of 1 T, field increments up to 0.4 mT, and averaging times of 100–300 ms. FORC diagrams were calculated using a program written by Tom Mullender at the Paleomagnetic Laboratory, Utrecht University. Data

representation close to the vertical axis of the FORC diagrams may be biased due to data extrapolation in this region. To avoid uncertain interpretation in this poorly defined part of the FORC space, it is not considered by the software. A smoothing factor (SF) between 3 and 5 was used. IRM acquisition curves were obtained by measuring 100–150 logarithmically spaced field steps up to a maximum field of 1 T on the AGM. IRM curves for some magnetically weak samples were measured using standard paleomagnetic core samples ($\sim 2 \times 2.5$ cm) on a robotized superconducting rock magnetometer (noise level $1–2 \times 10^{-12}$ Am^2) at Utrecht University. Sixty data points were measured up to 700 mT. IRM acquisition curves were decomposed into coercivity components using the fitting protocol of *Kruiver et al*. [2001].

Thermomagnetic runs were measured in air with a modified horizontal translation-type Curie balance with a sensitivity of $\sim 5 \times 10^{-9}$ Am^2 [*Mullender et al*., 1993] at Utrecht University. The applied field was cycled between 100 and 300 mT. Multiple heating and cooling cycles between room temperature, 200, 300, 350, 450, 620, and 700°C were performed at a heating/cooling rate of 6°C/min. Depending on sample magnetization, ~10–100 mg of sediment was used. A quartz glass holder and quartz wool were used to hold samples. Low-temperature magnetic properties were measured with a Quantum Design Magnetic Property Measurement System (MPMS; model XL7) at the Australian National University (ANU). For zero-field cooled (ZFC) and field-cooled (FC) curves, samples were cooled to 10 K in either zero-field or a 5 T field. At 10 K, a 5 T field was applied and then switched off to impart a low-temperature saturation IRM (SIRM), and the MPMS magnet was reset (the residual field after a magnet reset is ~200–300 μT). SIRM warming curves were measured during warming in zero-field. ZFC warming curves were acquired before the FC curves.

Ferromagnetic resonance (FMR) spectroscopy is used widely to detect biogenic magnetite chain signatures [e.g., *Weiss et al*., 2004; *Kopp et al*., 2006, 2007; *Roberts et al*., 2011b, 2012; *Chang et al*., 2014] and was employed to study our greigite-bearing samples. X-band FMR spectra were measured with a JEOL electron paramagnetic resonance (EPR) spectrometer at the Technical University of Munich or a Bruker Elexys EPR spectrometer at ANU. The 30–100 mg of sediment was measured at a frequency of 9.1–9.4 GHz and power of 0.6–2 mW. We used the same FMR parameters as those in other studies [*Kopp et al*., 2006; *Roberts et al*., 2011b, 2012].

Magnetic particles were extracted from bulk sediments by adapting the methods of *Petersen et al*. [1986] and *Vasiliev et al*. [2008]. Approximately 10 g of ground sediment was mixed with 300 mL of argon-purged demineralized water. Sodium polyphosphate ($Na_4P_2O_7 \cdot 10H_2O$) was added to disperse the clays. The sediment solution was agitated using an ultrasonic bath for 30 min. The obtained sediment suspension was circulated through a Frantz isodynamic magnetic separator for several hours. Magnetic extracts were then washed several times with demineralized water using a bar magnet. Magnetic extracts were viewed and analyzed using either a FEI Tecnai 20 FEG TEM at an acceleration voltage of 200 kV at Utrecht University, or a Philips CM300 TEM operated at 300 kV at ANU. Elemental compositions and crystal structures were analyzed using energy dispersive spectroscopy (EDS) and selected-area electron diffraction (SAED).

XRF analysis was carried out using a Thermo Scientific Niton XL3t XRF Analyzer at Utrecht University. Measurements were made on the top surface of standard paleomagnetic cylindrical samples. One flat surface of the cylinder was cleaned directly prior to data acquisition to ensure that data were obtained from fresh samples. Three measurements were averaged. Data that were significantly different from other measurements (e.g., when the X-ray beam interacted with large fossil shells) were excluded and measurements were repeated. Our XRF analysis is semiquantitative because no standard samples were used for calibration. Our purpose is to track elemental trends through the sequence, rather than absolute elemental concentrations. There are good correlations between large-scale elemental variations and magnetic properties, which are expected to reflect real sedimentary variations.

Samples from the Zheleznyi Rog section were taken at ~1–2 m stratigraphic intervals for paleomagnetic analysis [*Krijgsman et al*., 2010; *Vasiliev et al*., 2011]. Sister paleomagnetic samples were used for rock magnetic, XRF, and electron microscopic analyses. A total of ~150 samples from Taman (selected from the 0–230 m stratigraphic interval) were measured for hysteresis properties, IRM acquisition and backfield curves, and XRF elemental variations; ~40 were measured for FORC diagrams, ~20 were selected for thermomagnetic analyses, and 6 were selected for low-temperature magnetic analyses, FMR, and TEM observation. For samples from Romania, ~20 paleomagnetic drill core sister samples [*Vasiliev et al*., 2004, 2005, 2008] were selected for hysteresis, IRM, FORC, FMR, and thermomagnetic analyses.

4. Results

4.1. Rock Magnetism

4.1.1. Hysteresis Properties and FORC Diagrams

The studied samples have a wide range of hysteresis properties, mostly with single domain (SD) behavior (Figures 3a–3c). One type of hysteresis loop has relatively square shapes with M_{rs}/M_s ratios of ~0.28–0.43 and B_c values of ~10–25 mT (Figure 3a). The other type has high B_c values (mostly between 40 and 50 mT) and high M_{rs}/M_s ratios up to ~0.7, which are dominated by cubic magnetocrystalline anisotropy [*Roberts*, 1995] (Figure 3b). Some samples have intermediate B_c and M_{rs}/M_s values mostly between these two types of hysteresis loops (Figure 3c). We classified the studied SD-dominated samples into three groups by their hysteresis and FORC characteristics: type-A (lower B_c and square loops), type-B (higher B_c), and type-C (intermediate between type-A and type-B). We use this classification consistently throughout this paper. Hysteresis ratios for some samples are plotted after *Day et al*. [1977] in supporting information Figure S1.

High-resolution FORC measurements indicate variable coercivity and magnetostatic interaction distributions (Figures 3d–3f). Type-A samples (Figure 3d) have a dominant narrow ridge along the B_i axis with negligible vertical spread. This FORC signature corresponds to that of noninteracting or weakly interacting SD particles [*Pike et al*., 1999; *Egli et al*., 2010]. Type-B samples have FORC diagrams (Figure 3e) with concentric contours with large vertical spread indicative of strong magnetostatic interactions [*Pike et al*., 1999; *Roberts et al*., 2000]. FORC diagrams for type-C samples have a mixture of type-A and type-B signatures: with both a central ridge and vertically spread concentric contours (Figure 3f). These samples, therefore, contain a variable mixture of noninteracting and interacting SD particles. FORC measurements for the same type-C samples measured with different numbers of FORCs but covering the same FORC region indicate that the central ridge signature is not clear in low-resolution FORC diagrams (Figures S2a and S2b), but it becomes more clearly evident in high-resolution FORC diagrams (Figures S2c and S2d).

4.1.2. IRM Acquisition and Demagnetization

Coercivity of remanence (B_{cr}) values, determined from backfield demagnetization measurements, range between ~30 and 70 mT. IRM acquisition curves for most samples can be fitted [*Kruiver et al*., 2001] with two main components (Figures 3g–3i). For type-A samples, one IRM component has a median field of ~50–70 mT and a small fitted dispersion parameter (DP) in the range of 0.20–0.22 (Figure 3g, magenta line). This component contributes ~55–80% of the total IRM. The other IRM component has a smaller median field (~25–36 mT) and broader distribution (DP = ~0.45–0.48) (Figure 3g, green line). Type-B samples also have two major IRM components, one with a narrow distribution (Figure 3h, magenta line) and the other with a broad distribution (Figure 3h, green). The narrow IRM component for type-B samples contributes ~60–70% of the total IRM intensity. Compared to type-A samples, the narrow IRM component for type-B samples has higher median field (mostly between ~75 and 80 mT). DP values for this component are even smaller (mostly between 0.13 and 0.16). The other major component with broader distribution for type-B samples has median field values of ~40–67 mT, and DP values of ~0.32–0.36. Type-C samples (Figure 3i) have IRM components similar to type-B samples. All types of samples have an IRM component with DP < 0.22. The small low-field IRM component for all types of samples likely reflects deviations of the major IRM component from an ideal lognormal model distribution [*Egli*, 2004], to which we do not attribute physical meaning. This "skewed-to-the-left" behavior requires an extra component if fitting is restricted to symmetric distributions [*Kruiver et al*., 2001].

4.1.3. High and Low-Temperature Magnetic Properties

Thermomagnetic runs in air during different heating and cooling cycles indicate an irreversible decrease in magnetization between 200 and 400°C with most pronounced drops in magnetization from ~350 to 420°C in many samples (Figures 3j–3l). An irreversible decrease in magnetization between 200 and 420°C is indicative of greigite [e.g., *Reynolds et al*., 1994; *Roberts*, 1995; *Dekkers et al*., 2000; *Vasiliev et al*., 2008; *Chang et al*., 2008; *Roberts et al*., 2011a] and is not characteristic of stoichiometric magnetite. For oxidized magnetite, such as magnetite with a maghemite (γ-Fe_2O_3) coating, further oxidation occurs during heating in air, which causes irreversible magnetization loss. However, this loss is much less pronounced. Most samples also undergo a magnetization increase starting at ~400°C, with a peak at ~500°C, which indicates formation of a new magnetic mineral (most likely magnetite) due to oxidation of iron sulfides (usually pyrite) [*Passier et al*., 2001]. Variations in the magnitude of this high-temperature peak with respect to the magnetization

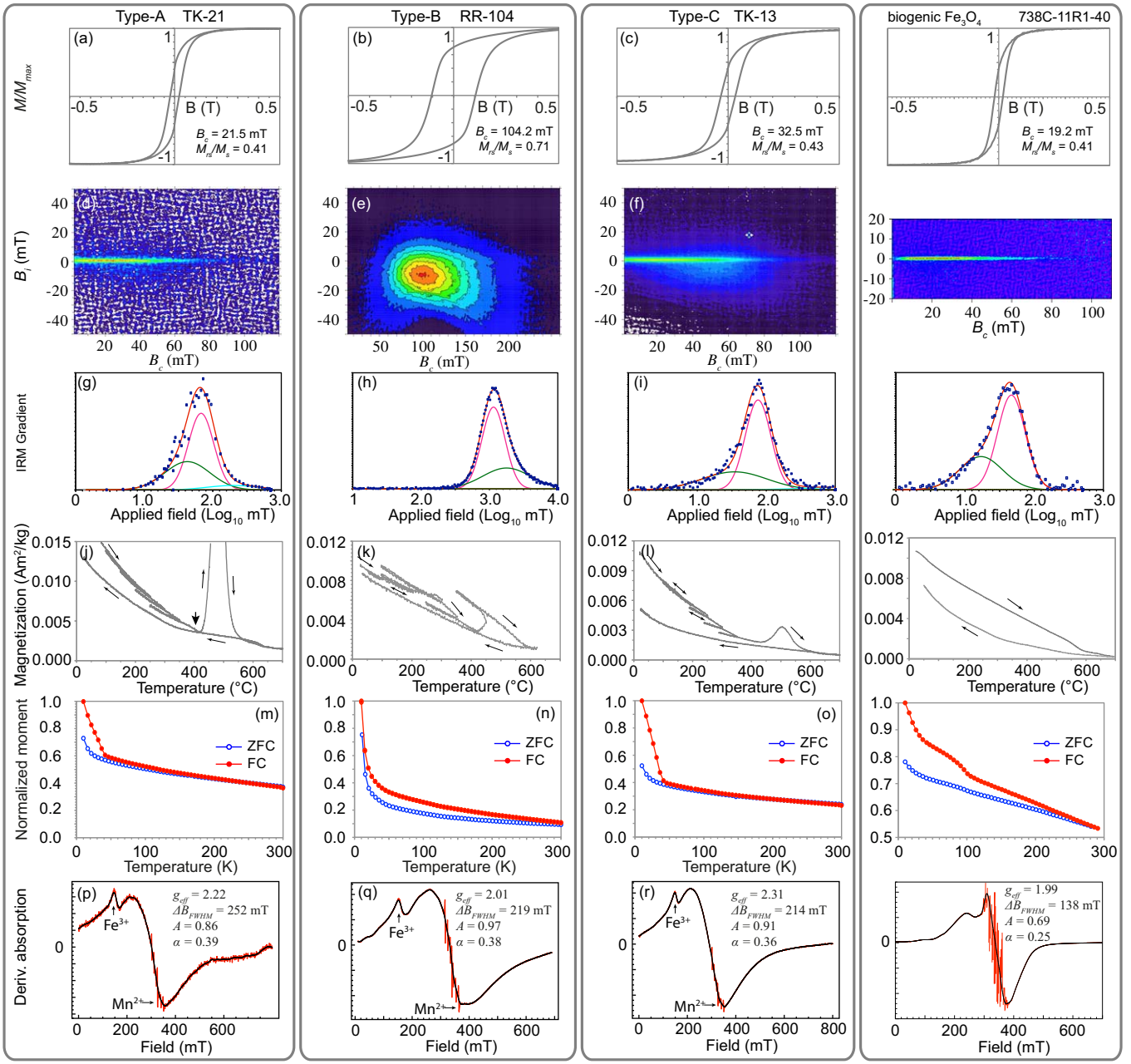

Figure 3. Comparison of rock magnetic results for three types of studied greigite samples and a biogenic magnetite sample. (a–c) Hysteresis loops, (d–f) FORC diagrams, (g–i) IRM component analyses, (j–l) thermomagnetic curves, (m–o) low-temperature ZFC-FC curves, and (p–r) FMR spectra. A fourth column contains magnetic data for typical magnetite magnetofossil-bearing sediment (sample "738C-11R1–40") from the Palaeocene-Eocene thermal maximum, ODP Hole 738C [*Larrasoaña et al.*, 2012]. All hysteresis loops (Figures 3a–3c) are normalized to M_s values (at 1 T) after paramagnetic slope correction. Hysteresis parameters (B_c and M_{rs}/M_s), determined from the entire loop to ±1 T, are indicated. FORC diagrams for type-A samples with a narrow central ridge along the B_i axis, with negligible vertical spread, are indicative of negligible magnetostatic interactions. FORC diagrams for type-B samples have concentric contours and a large vertical spread. Type-C samples have mixed FORC signatures from both noninteracting and interacting components. For results of IRM component analyses (Figures 3g–3i), squares indicate measured data. Red lines are the fitted total spectra. The other lines (magenta, green, and blue) are different components with lognormal coercivity distributions. Thermomagnetic runs (Figures 3j–3l) were measured in air during multiple heating and cooling cycles (arrows). All samples produce an irreversible magnetization decrease below 400°C, due to greigite decomposition. The peak at ~500°C is due to oxidation of pyrite into magnetite [*Passier et al.*, 2001]. In the low-temperature magnetic data (Figures 3m–3o), FC and ZFC SIRM warming curves are indicated by red solid circles and blue open circles, respectively. The magnetizations are normalized to the FC data at 10 K. No clear Verwey transition is observed. In the FMR spectra (Figures 3p–3r), arrows indicate paramagnetic high-spin Fe^{3+} signals ($g = 4.3$) and Mn^{2+} sextet signals. Raw data are shown in red. Black lines are smoothed curves that reduce the effects of the sharp Mn^{2+} EPR sextet signals and noise. FMR parameters for each measured sample are shown.

loss below 400°C probably indicates variable concentrations of pyrite and greigite within the studied samples. Cooling from 700°C indicates that most of the newly formed magnetite transformed into hematite during heating.

We measured hysteresis properties and FORC diagrams for a range of samples at room temperature after heating to different temperatures and compare these with room temperature measurements without heating (Figure S3). After heating to 400°C, the characteristic noninteracting FORC signature for greigite-bearing sediments disappears (Figure S3a). Thermal decomposition of greigite below 400°C has been widely documented [e.g., *Skinner et al*., 1964; *Reynolds et al*., 1994; *Roberts*, 1995; *Dekkers et al*., 2000; *Vasiliev et al*., 2008; *Chang et al*., 2008; *Roberts et al*., 2011b]. In contrast, hysteresis loops and FORC diagrams for samples known to contain magnetite magnetofossils remain nearly the same after heating to 400°C (Figures S3b and S3c).

Low-temperature magnetic measurements indicate a nearly continuous decrease in remanence upon warming. No clear Verwey transition (T_v) is detected (Figures 3m–3o). This is consistent with the presence of greigite [*Moskowitz et al*., 1993; *Roberts*, 1995; *Chang et al*., 2009] and precludes the presence of significant magnetite within our samples. The large divergence between ZFC and FC curves below 35 K for samples from Taman (Figures 3m and 3o) is consistent with the magnetic behavior of siderite ($FeCO_3$) [*Housen et al*., 1996; *Frederichs et al*., 2003], which is a common authigenic mineral in reducing diagenetic sedimentary environments. This low-temperature discontinuity at 35 K is not due to the magnetic behavior of monoclinic pyrrhotite (Fe_7S_8) [*Dekkers et al*., 1989; *Rochette et al*., 1990], as no discontinuity around 35 K is observed during low-temperature cycling of a room temperature SIRM.

4.2. FMR Spectroscopy

Room temperature FMR spectra for selected samples are presented in Figures 3p–3r. Most measured samples have a peak at a *g* value of 4.3 due to paramagnetic high-spin Fe^{3+}, and a characteristic Mn^{2+} sextet signal (labeled in Figures 3p–3r). The Mn^{2+} and paramagnetic Fe^{3+} signals are not of interest in this study and were therefore removed before calculating the FMR parameters. The residual FMR spectra for all types of samples have only one low-field peak and one broad high-field peak (Figures 3p–3r). These spectra contrast with those for intact biogenic magnetite [*Weiss et al*., 2004; *Kopp et al*., 2006, 2007; *Roberts et al*., 2011a, 2012; *Larrasoaña et al*., 2012]. Particularly, they lack the multiple low-field absorption peaks and sharp high-field peak. These samples have g_{eff} of 2.0–2.3, ΔB_{FWHM} values of 210–250 mT, asymmetric ratio *A* values close to 1, and α values larger than 0.3 (0.36–0.39). These FMR parameters do not fall within the regions for magnetite magnetosome chains [*Weiss et al*., 2004; *Kopp et al*., 2006].

4.3. TEM Observations

TEM observations were performed on magnetic extracts for both type-A and type-C samples (where a central ridge FORC feature is found) from the Black Sea sequence at Taman. Abundant iron sulfide nanocrystals are observed (Figures 4a–4c), which have been confirmed by EDS analysis (Figures 4j–4l). SAED patterns on selected extracted crystals are consistent with the crystal structure of greigite. Most crystals have octahedral, prismatic, round, or irregular shapes (Figure 4). Some greigite crystals have sizes and morphologies that are consistent with biogenic greigite crystals observed in living MTB, i.e., octahedral, cubo-octahedral, prismatic, and roundish, with a size range of ~20–100 nm and average size of ~60–75 nm [*Farina et al*., 1990; *Mann et al*., 1990; *Bazylinski et al*., 1995; *Kasama et al*., 2006; *Muxworthy et al*., 2013], which suggests a biogenic origin. Iron oxides (Figure 4d) are rare. This is consistent with bulk magnetic measurements, which indicate that greigite, rather than magnetite, is the main magnetic mineral in these sediments.

TEM-EDS analysis indicates the common presence of nickel (Figure 4l) within some larger iron sulfide crystals (100–500 nm). The ratio of Fe and Ni peak areas in TEM-EDS spectra is large (~38, 23, 11, and 5 for four crystals), which indicates variable Fe-Ni composition. In order to determine the Fe-Ni-bearing sulfide mineral phase, SAED patterns (Figures 4f–4i) were recorded on several representative Fe-Ni sulfide crystals, including the one in Figure 4e. The distinct crystal structure of greigite (cubic; space group $Fd\bar{3}m$), pyrite (cubic; space group $Pa\bar{3}$), and other common iron sulfide minerals (mackinawite: tetragonal *P4/nmm*; monoclinic pyrrhotite: *A2/a*) makes them readily distinguishable using SAED analysis. All measured diffraction patterns are consistent with those expected for the cubic crystal structure of greigite (Figures 4f–4i). Diagenetic iron-nickel sulfides have only been reported from Plio-Pleistocene marine marls from the Vrica section, Calabria, Italy [*Van Velzen et al*., 1993]. However, *Van Velzen et al*. [1993] could not provide crystal structure identification along with their microprobe analyses of this Fe-Ni-S phase, and they suggested monoclinic pyrrhotite as a possible mineral phase. Ni substitution in diagenetic magnetic minerals has not been confirmed by follow-up studies of the Vrica section [*Roberts et al*., 2010], and it has not been observed elsewhere in greigite [*Roberts et al*., 2011a]. Our TEM-based chemical and structural analysis confirms, for the first time, that

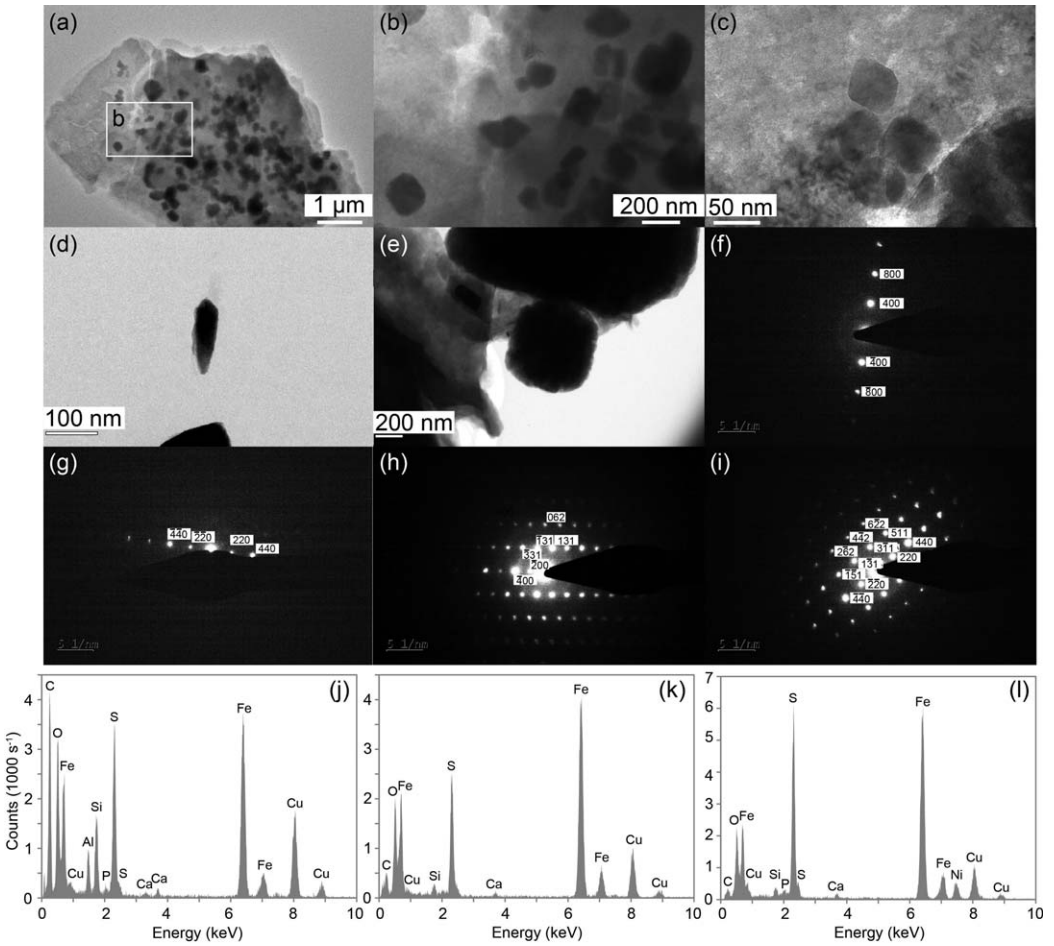

Figure 4. Bright field TEM images of magnetic mineral extracts from sediment samples from Taman, Russia, (a and b) for a type-C sample "TK-13" and (c and d) for a type-A sample "TK-25." The crystals in Figures 4a–4c are iron sulfides. A single bullet-shaped biogenic magnetite crystal (Figure 4d). (e) A representative Fe-Ni sulfide crystal identified within sample "TK-13." (f–i) SAED patterns for several representative Fe-Ni sulfide crystals. All the diffraction patterns are consistent with those expected for the cubic structure of greigite. Miller hkl indices are indicated. Measured d-spacings: in Figure 4f, (400): 2.4 Å; in Figure 4g, (220): 3.5 Å; in Figure 4h, (200): 4.9 Å, (131): 3.0 Å, (062): 1.6 Å; and in Figure 4i, (220): 3.5 Å, (131): 3.0 Å, (442): 1.7 Å. (j, k) Selected EDS spectra of crystals in Figures 4b and 4c. Both spectra contain large Fe and S peaks. (l) EDS spectrum for the isolated crystal in Figure 4e, which has a Ni signal in addition to the large Fe and S peaks and is common in the studied iron sulfide crystals. Cu and C signals originate from the TEM grid. Other peaks, e.g., Si, Al, O, and P, etc., probably originate from the clay mineral flakes.

diagenetic Fe-Ni sulfides have a ferrimagnetic greigite structure, although diagenetic formation of cation-doped greigite and its effects on the magnetization of greigite-bearing sediments need further investigation.

5. Discussion

5.1. Magnetic Identification of Biogenic Greigite and Paleomagnetic Implications

Biogenic magnetite produced by MTB has a range of distinct properties, such as characteristic crystal morphologies, narrow particle size distribution, chain structure, and SD magnetic behavior, which can be used to discriminate it from other types of magnetic minerals. Biogenic magnetite can be identified by direct TEM observations of magnetic mineral extracts and by a range of magnetic methods, including low-temperature magnetic tests [*Moskowitz et al*., 1993, 2008; *Weiss et al*., 2004; *Chang et al*., 2013], IRM analysis [*Kruiver and Passier*, 2001; *Egli*, 2004], FMR spectroscopy [*Weiss et al*., 2004; *Kopp et al*., 2006; *Roberts et al*., 2012], and FORC diagrams [*Egli et al*., 2010; *Roberts et al*., 2011b, 2012]. In contrast, detection of biogenic greigite is expected to be more difficult. First, biogenic greigite crystals tend to have less regular morphologies [e.g., *Farina et al*., 1990; *Mann et al*., 1990; *Pósfai et al*., 1998a, 1998b; *Kasama et al*., 2006] compared to

the distinct crystal morphologies of bacterial magnetite [*Petersen et al*., 1986; *Stoltz et al*., 1986; *Roberts et al*., 2011b; *Chang et al*., 2012; *Larrasoaña et al*., 2012; *Yamazaki*, 2012]. Sedimentary diagenesis can also produce inorganic greigite crystals with a large grain-size spectrum [*Pósfai et al*., 2001; *Rowan and Roberts*, 2006; *Roberts et al*., 2011a] that includes the narrow size range of biogenic greigite crystals [*Farina et al*., 1990; *Mann et al*., 1990]. These factors make biogenic greigite crystal morphologies much less distinctive of biogenicity. Moreover, the often nonideal chain architecture of biogenic greigite [*Farina et al*., 1990; *Mann et al*., 1990; *Pósfai et al*., 1998a, 1998b; *Kasama et al*., 2006] compared to biogenic magnetite, and the absence of a low-temperature phase transition for greigite [*Moskowitz et al*., 1993; *Roberts*, 1995; *Chang et al*., 2009] mean that magnetic protocols for identifying biogenic magnetite may not be applicable to biogenic greigite. Additionally, extraction of magnetic minerals from lithified sedimentary rocks will cause significantly more disruption of magnetosome chain structures than in unconsolidated sediments and poorly cemented rocks.

Reinholdsson et al. [2013] observed that greigite magnetofossil-bearing Baltic sapropels have a FORC central ridge signature similar to that of biogenic magnetite. Biogenic magnetic minerals (both greigite and magnetite) preserved as isolated chains within sediment matrix are magnetically equivalent to noninteracting uniaxial SD particles. Such particle systems produce FORC distributions with a central ridge signature that has often been observed for intact biogenic magnetite chains [*Egli et al*., 2010; *Roberts et al*., 2011b, 2012]. In contrast, sedimentary diagenesis usually produces close-packed three-dimensional greigite clusters [e.g., *Jiang et al*., 2001; *Roberts and Weaver*, 2005; *Rowan and Roberts*, 2006; *Sagnotti et al*., 2010]. This distinct microstructure of diagenetic greigite results in strong magnetostatic interactions that produce FORC diagrams with significant vertical spread [*Roberts et al*., 2000, 2006; *Rowan and Roberts*, 2006; *Chang et al*., 2007; *Vasiliev et al*., 2007]. This type of FORC diagram has two other features: (1) the center of the distribution is shifted downward to negative B_i values; and (2) there is a negative peak close to the B_i axis in the lower quadrant. These signatures all indicate a strongly interacting SD magnetic particle assemblage [*Pike et al*., 1999; *Roberts et al*., 2000; *Newell*, 2005]. Such FORC signatures are observed for type-B and type-C samples that contain diagenetic greigite and are absent for type-A samples (biogenic origin). FORC diagrams, therefore, appear to be an excellent tool for discriminating biogenic from diagenetic greigite (Figures 3d–3f) [see also *Reinholdsson et al*., 2013]. We do not know the exact configuration of biogenic greigite crystals in sediments due to magnetic extraction-induced disruptions. Although fossilized biogenic greigite chains in sediments may not be well preserved, greigite magnetofossils cannot form close-packed particle clusters. Such distinct crystal arrangements, i.e., intact or disrupted biogenic greigite chains compared to diagenetic greigite in close-packed grain clusters, produce distinct magnetostatic interactions and FORC diagrams. FORC diagrams for some of our studied samples contain a central ridge (Figures 3d, 3f, and S1). This central ridge feature is unlikely to be due to initial growth of diagenetic greigite because early diagenetic greigite normally contains ultrafine particle clusters, with dominantly superparamagnetic properties and strong magnetostatic interactions [*Rowan et al*., 2009]. Such properties would not produce a central ridge feature. The central ridge signature also cannot be due to isolated greigite particles because greigite has cubic symmetry that would produce some vertical spread in FORC diagrams.

Our identification of biogenic greigite is supported by TEM observations that indicate the presence of abundant greigite nanocrystals, whose size and morphology are consistent with a biogenic origin (Figure 4). In addition, samples with a dominant central ridge feature (type-A) do not acquire a gyroremanent magnetization (GRM) during alternating field (AF) demagnetization [*Krijgsman et al*., 2010; *Vasiliev et al*., 2011]. This GRM behavior contrasts with diagenetic greigite samples, which often contain closely packed greigite crystals that produce a bias field that enable GRM acquisition. No clear T_v is detected (Figures 3m–3o), and thermal demagnetization of the natural remanent magnetization (NRM) on the same samples indicates that almost all remanence was removed below 420°C [*Krijgsman et al*., 2010; *Vasiliev et al*., 2011]. These observations indicate that there is no significant magnetite concentration in the studied samples.

FMR analysis provides another powerful tool for detecting biogenic magnetite chains [*Weiss et al*., 2004; *Kopp et al*., 2006]. We did not obtain a positive FMR test for our greigite-bearing samples (Figures 3p–3r). This may be due to the fact that greigite magnetosome chains often have less regularly arranged crystal orientations and chain alignment [*Kasama et al*., 2006]. Some greigite-producing MTB strains, such as magnetotactic rods and multicellular magnetotactic prokaryotes, have two or more adjacent chains. Significant departure from ideal linear chain structures—which is often found in intact greigite magnetosomes—will result in effective demagnetization and weaken the shape anisotropy. Such reduced shape anisotropy

would produce lower coercivities in biogenic greigite and cause a more gradual change in magnetization state, as has been confirmed by remanence measurements on single greigite-producing bacterial cells [*Penninga et al*., 1995; *Winklhofer et al*., 2007] and hysteresis measurements on greigite magnetofossil-bearing sapropels [*Reinholdsson et al*., 2013].

Small DP values for IRM coercivity components have been used as an indicator of biogenic magnetite [*Kruiver and Passier*, 2001; *Egli*, 2004]. Biogenic greigite, which also has a narrow grain size distribution [*Pósfai et al*., 2001; *Kasama et al*., 2006], is expected to produce small DP values, as observed in our type-A biogenic greigite samples (Figure 3g). In contrast to natural greigite samples (Figures 3g–3i), hydrothermally synthesized greigite samples [*Chang et al*., 2007, 2008] have one coercivity component with an ideal lognormal distribution and large DP values (0.31–0.33) (Figure S4). This is consistent with the fact that the hydrothermal synthesis method used produces particles with a wide range of grain sizes [*Chang et al*., 2007, 2008]. However, diagenetic SD greigite samples produce even smaller DP values (Figures 3h and 3i). The origin of such small DP values is not clear. It is possible that the nearly touching grains in diagenetic greigite clusters represent a strongly coupled magnetic system, where exchange coupling between neighboring crystals becomes important and results in collective switching of the magnetization, i.e., if one particle switches, all other particles switch due to exchange coupling. Nevertheless, our results indicate that a small DP value is not a unique indication of magnetosome crystals.

Despite the global occurrence of greigite-producing MTB in modern anoxic aquatic environments, fossilized greigite magnetosomes have not been widely reported in the geological record. In contrast, preservation of diagenetic greigite in the global sedimentary geological record has been firmly established [*Roberts et al*., 2011a], dating back to the latest Precambrian [*Dong et al*., 2013]. This indicates that greigite can have a much higher preservation potential than was previously thought. While magnetite magnetosomes are prone to dissolution under sulfate-reducing diagenetic conditions, greigite magnetofossils should be stable in such sedimentary environments because such conditions are required for authigenic greigite formation. Rock magnetic analysis of the studied Romanian sediments also indicates that many samples contain a mixture of diagenetic and biogenic greigite (Figure S5). This supports the observations of two populations of greigite (diagenetic and biogenic) [*Vasiliev et al*., 2008]. Our observation of biogenic greigite signatures from the former Black Sea in Russia and Romania indicate their potential widespread occurrence in ancient sediments. Our identification of biogenic greigite signatures in sulfide-rich sedimentary environments demonstrates a high preservation potential for greigite magnetofossils.

Quantitative analysis of rates of geological processes cannot progress without precise chronology. Magnetostratigraphy is an important dating tool [*Langereis et al*., 2010], the reliability of which can be hampered by diagenetic greigite occurrences when greigite grows during later burial and erases and/or overprints the primary paleomagnetic signal [e.g., *Roberts and Weaver*, 2005; *Roberts et al*., 2010; *Sagnotti et al*., 2010]. Greigite magnetofossils, however, should record an early paleomagnetic signal because greigite-producing MTB often live close to the sediment-water interface or in the water column [e.g., *Bazylinski et al*., 1995; *Moskowitz et al*., 2008; *Lefèvre et al*., 2011; *Wang et al*., 2013], thus recording a quasi-primary NRM. Discrimination of biogenic from diagenetic greigite, therefore, has important implications for assessing the reliability of sedimentary paleomagnetic signals. Our analyses of magnetic carriers within the studied Black Sea sediments reinforces the interpretation that reliable paleomagnetic records can be obtained from such settings [*Vasiliev et al*., 2008, 2011; *Krijgsman et al*., 2010].

5.2. Environmental and Climatic Control of Diagenetic Greigite Formation: Competition Between Reactive Iron and Dissolved Sulfate

Our integrated analysis, combining rock magnetism, XRF geochemistry, and sedimentary cyclicity, on Black Sea sediments from the Taman Peninsula enables unraveling of potential environmental control on diagenetic greigite formation (Figure 5). Diagenetic greigite usually forms as closely packed three-dimensional grain clusters in sediments, which produce a range of distinct rock magnetic properties that can be readily detected [*Roberts et al*., 2011a]. These magnetic characteristics include SD hysteresis properties, large coercivity values (often $>$35 mT), high M_{rs}/M_s ratios ($>\sim$0.4), FORC diagrams indicative of strongly interacting assemblages, and GRM acquisition during AF demagnetization [*Roberts et al*., 2011a]. Biogenic greigite (type-A) at Taman is less abundant than diagenetic greigite, and is mostly identified within the $\sim$100–120 m interval (Figure 5). Diagenetic greigite (both type-B and type-C) occurs throughout the section, and

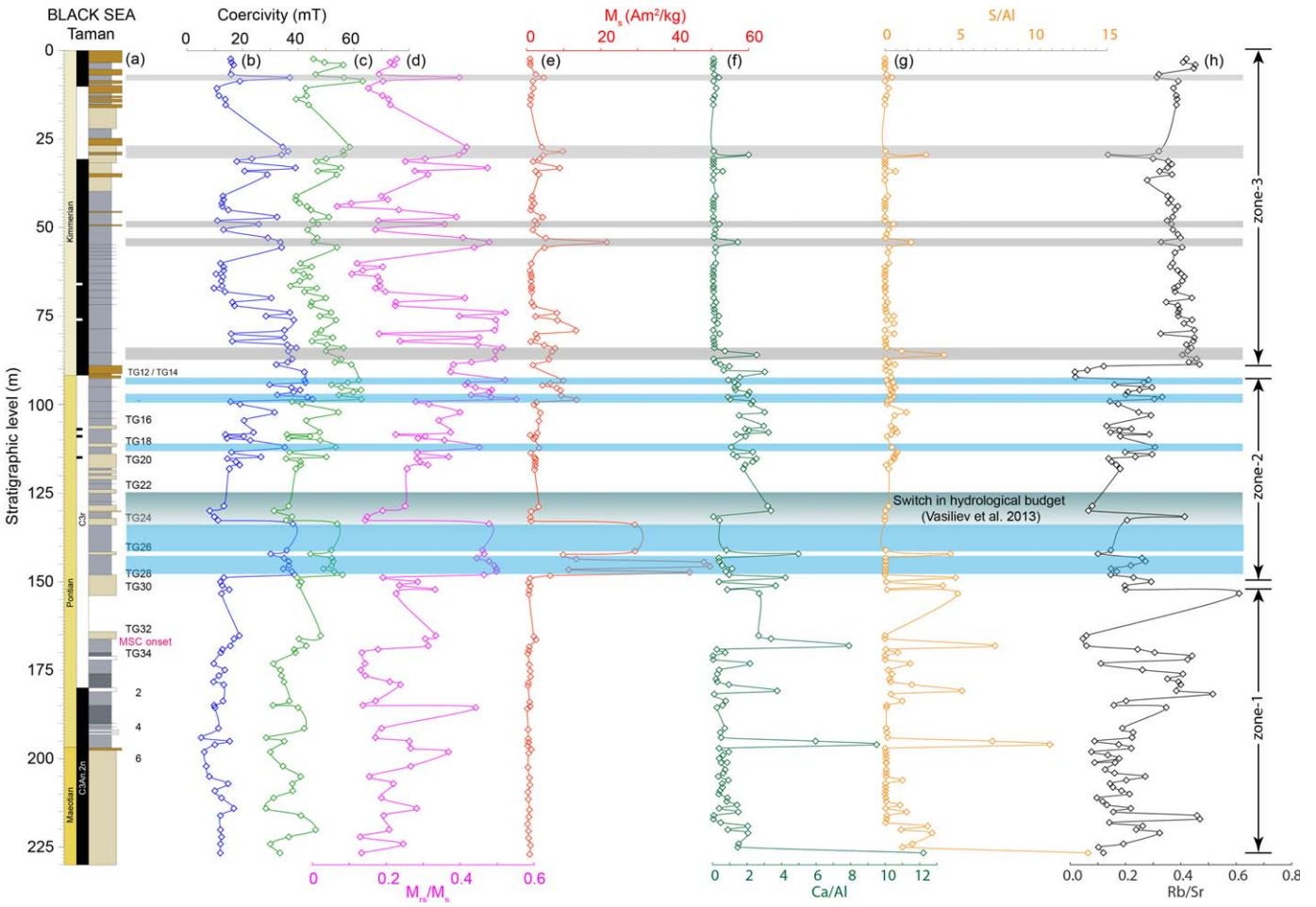

Figure 5. Magnetic and elemental variations in the Zheleznyi Rog section. (a) Lithology and paleomagnetic polarity, (b–e) rock magnetic properties, and (f–h) selected elemental ratios. Paleomagnetic polarities are from *Krijgsman et al.* [2010] and *Vasiliev et al.* [2011]. The polarity change at the red layer (stratigraphic level of ~90 m) is probably associated with a sedimentary hiatus at the MSC climax [*Krijgsman et al.*, 2010]. A significant change in hydrological budget in the Black Sea [*Vasiliev et al.*, 2013] is indicated. Magnetic properties with high values for (b) B_c, (c) B_{cr}, (d) M_{rs}/M_s, and (e) M_s are indicative of significant diagenetic greigite concentrations. Diagenetic greigite spikes (shading) occur occasionally (between 0 and ~150 m). Within zones 2 and 3, good correlations between diagenetic greigite concentration, lithology, and elemental abundances are identified (horizontal bars). In zone 3, diagenetic greigite concentration correlates to low Rb/Sr and high Ca/Al ratios (gray bars). In zone 2, diagenetic greigite spikes occur at intervals with high Rb/Sr and low Ca/Al (blue bars). Between 150 and 230 m (zone 1), samples are magnetically weak and lack any indication of greigite. The climatic index TG is from *Van der Laan et al.* [2005, 2006], which is the same as in Figure 2.

is common in clay-rich dark layers and absent in carbonate-rich light layers (Figures 2 and 5). We use $B_c > 35$ mT and M_s peaks as indicators of significant diagenetic greigite concentrations (horizontal bars; Figure 5). Biogenic greigite occurrences do not affect our paleoenvironmental interpretation for diagenetic greigite formation because diagenetic greigite typically has higher B_c and M_{rs}/M_s values than biogenic greigite (Figures 3a–3f) [*Reinholdsson et al.*, 2013].

Stratigraphic elemental variations, expressed as relative concentrations, indicate two distinct zones (zone 3 versus zones 1 and 2 in Figure 5) separated by the reddish layer associated with the MSC climax at ~89–94 m (Figures 2 and S6). Across the red layer, a distinct switch in some elemental contents and ratios (Ca, Ti, Ca/Al, and Rb/Sr; Figures 5 and S6) indicates a significant environmental change. In zone 1 (~150–230 m), samples are magnetically weak (dominantly paramagnetic) and lack diagenetic greigite. Zone 2 (below the reddish layer) is characterized by generally high Ca/Al ratios and low Rb/Sr, compared to zone 3. Contrasting diagenetic greigite concentrations and geochemical parameters occur in zones 2 and 3. In zone 2, blue bars in Figure 5 indicate high B_c and M_s values (which indicate significant diagenetic greigite concentrations) correlate with low Ca/Al (i.e., weaker biogenic activity) and S/Al (i.e., less sulfidic sulfur) ratios, but high Rb/Sr (stronger continental weathering and more terrigenous input) [*Blanchet et al.*, 2009]. In zone 3, high B_c and M_s values are indicated with gray shading in Figure 5, where they correlate with high Ca/Al and S/Al ratios, but low Rb/Sr.

In sulfate-reducing sedimentary environments, greigite forms as a precursor to pyrite through reaction of detrital iron-bearing minerals with H_2S (produced by sulfate-reducing bacteria). These reactions are often limited by three principal factors: (1) availability of dissolved sulfate in sedimentary pore waters, (2) availability and reactivity of organic matter for microbial metabolism, and (3) reactive iron released from detrital minerals [*Berner*, 1984; *Roberts et al*., 1996; *Roberts and Weaver*, 2005]. *Kao et al*. [2004] demonstrated that HS^- released by microbes can be effectively removed by high dissolved iron activity (i.e., from abundant reactive detrital iron-bearing minerals or coatings from which Fe^{2+} dissolves), so that the pathway to pyrite formation is arrested and intermediate greigite is preserved. A similar mechanism was invoked by *Blanchet et al*. [2009] to explain the formation and preservation of diagenetic greigite in rapidly deposited marine sediments from the Santa Barbara Basin, where diagenetic greigite occurs in terrigenous-rich and organic-poor sedimentary layers. In such a scenario, diagenetic greigite peaks should correlate with high Rb/Sr and low Ca/Al ratios (stronger continental detrital contribution and weaker biogenic activity). This pattern is observed in zone 2 of the studied sediments (Figure 5, blue bars), where diagenetic greigite formation appears to have been controlled mainly by terrigenous input. In marine sedimentary environments, sulfate is abundant and is readily used by microbes to produce H_2S (or HS^-). However, diagenetic greigite peaks also occur in intervals with lower continental detrital inputs in zone 3 (i.e., low Rb/Sr and high Ca/Al). In lake environments, detrital iron-bearing minerals and reactive organic matter are often abundant and, therefore, should not limit diagenetic greigite formation, but dissolved sulfate concentrations are typically low [*Roberts et al*., 1996]. It has been suggested that the key factor for diagenetic greigite formation in lacustrine environments is dissolved sulfate availability, with greigite preservation being favored by sulfate consumption before reaction to pyrite is completed [*Roberts et al*., 1996]. This appears to have been the case in zone 3, which is supported by thermomagnetic data (Figure S7), where samples from the weakly magnetized interval (i.e., low M_s and B_c values) in zone 3 contain a dominant paramagnetic signal with no indication of pyrite (i.e., a pyrite peak at ~500°C is absent [*Passier et al*., 2001]; Figure S7). In contrast, weak samples in zones 1 and 2 often have a pronounced pyrite peak at ~500°C (Figure S7). This is also consistent with the observation that diagenetic greigite peaks correlate with S/Al peaks.

Paleontological analysis of endemic Paratethys faunal assemblages (molluscs and ostracods) from the studied Taman section indicates an evolution from a marine to a lake environment across the MSC climax [*Krijgsman et al*., 2010]. This paleoenvironmental evolution is consistent with our interpretation of conditions that favored diagenetic greigite formation. Prior to the MSC climax, significant greigite formation probably coincided with climatic changes or sea level drops during the MSC. During this interval, diagenetic greigite formation occurred in warm/wet climatic periods (Figures 2 and 5) and was probably prompted by terrigenous enrichments in reactive iron supply driven by enhanced continental weathering around the Black Sea. After the MSC climax, the Black Sea basin was isolated and disconnected from the Mediterranean and became a large lake [*Krijgsman et al*., 2010]. During this period, diagenetic greigite enhancement was due to limnological conditions that caused small amounts of dissolved sulfide to react with abundant iron to cause greigite preservation. In summary, we observe contrasting environmental controls on diagenetic greigite formation between marine and lacustrine environments in the same sedimentary sequence. This supports a previous suggestion that diagenetic iron sulfides, including greigite, could be useful paleosalinity indicators [*Berner et al*., 1979].

6. Conclusions

We provide evidence for biogenic greigite preservation from Black Sea sediments in Russia and Romania. Biogenic greigite has magnetic properties that enable discrimination from other types of magnetic minerals, particularly diagenetic greigite. FORC analysis is the most useful method for identifying biogenic greigite: the central ridge signature of biogenic greigite contrasts with vertically distributed signatures for diagenetic greigite. High-temperature magnetic properties enable discrimination of greigite from magnetite due to thermal decomposition of greigite below 420°C. Our analysis suggests that preservation of greigite magnetofossils is potentially widespread in ancient sediments. Their high preservation potential is important for understanding the paleomagnetic reliability of greigite bearing sediments, which can be complicated by remagnetizations. In addition, our TEM analysis enabled identification of the common presence of nickel-doped iron sulfides, which we confirm to have a greigite structure.

Integrated rock magnetic, geochemical and cyclostratigraphic analysis of a sedimentary sequence from the Black Sea basin provides an improved age model for understanding the evolution of the Black Sea, particularly during the Messinian Salinity Crisis. We observe correlation between diagenetic greigite concentrations and certain geochemical features, which demonstrate an environmental control on diagenetic greigite formation. Prior to the MSC climax, the Black Sea basin in Taman was dominantly a marine environment that became progressively disconnected from the Mediterranean Sea. Greigite formation within this interval appeared to have been climatically controlled with greigite layers occurring during warm/wet periods, which are interpreted to have been associated with enhanced terrigenous input. After the MSC climax, the Black Sea basin became isolated from the Mediterranean Sea and a freshwater environment dominated. This environmental change altered the relative abundance of detrital iron minerals, organic matter and dissolved pore water sulfate that resulted in different authigenic greigite formation patterns. Our studies demonstrate the usefulness of magnetic analysis, particularly greigite detection, for paleoenvironmental reconstructions.

Acknowledgments
We thank Maxim Krasnoperov for laboratory assistance with magnetic measurements and magnetic mineral extraction, Tobia De Scisciolo and Nicole van den Berg for XRF measurements, and Carmen Haeßner at Munich Technical University and Rainer Grün at the Australian National University for help with FMR measurements. Silja Hüsing is thanked for helpful discussions. We are grateful to Ramon Egli, four anonymous reviewers, and Associate Editor Joshua Feinberg for constructive comments and Thorsten Becker for editorial handling. Data for this paper are available from the Magnetics Information Consortium (MagIC) database. This work was financially supported by the Netherlands Organization for Scientific Research (NWO) and the Australian Research Council (DP120103952 and DP140104544).

References

Bazylinski, D. A., and R. B. Frankel (2004), Magnetosome formation in prokaryotes, *Nat. Rev. Microbiol.*, *2*, 217–230.
Bazylinski, D. A., R. B. Frankel, B. R. Heywood, S. Mann, J. W. King, P. L. Donaghay, and A. K. Hanson (1995), Controlled biomineralization of magnetite (Fe_3O_4) and greigite (Fe_3S_4) in a magnetotactic bacterium, *Appl. Environ. Microbiol.*, *61*, 3232–3239.
Berner, R. A. (1984), Sedimentary pyrite formation: An update, *Geochim. Cosmochim. Acta*, *48*, 605–615.
Berner, R. A., T. Baldwin, and G. R. Holdren Jr. (1979), Authigenic iron sulfides as paleosalinity indicators, *J. Sediment. Petrol.*, *49*, 1345–1350.
Blanchet, C. L., N. Thouveny, and L. Vidal (2009), Formation and preservation of greigite (Fe_3S_4) in sediments from the Santa Barbara Basin: Implications for paleoenvironmental changes during the past 35 ka, *Paleoceanography*, *24*, PA2224, doi:10.1029/2008PA001719.
Cande, S. C., and D. V. Kent (1995), Revised calibration of the geomagnetic polarity time scale for the Late Cretaceous and Cenozoic, *J. Geophys. Res.*, *100*, 6093–6095.
Chang, L., A. P. Roberts, A. R. Muxworthy, Y. Tang, Q. Chen, C. J. Rowan, Q. Liu, and P. Pruner (2007), Magnetic characteristics of synthetic pseudo-single-domain and multi-domain greigite (Fe_3S_4), *Geophys. Res. Lett.*, *34*, L24304, doi:10.1029/2007GL032114.
Chang, L., A. P. Roberts, Y. Tang, B. D. Rainford, A. R. Muxworthy, and Q. Chen (2008), Fundamental magnetic parameters from pure synthetic greigite (Fe_3S_4), *J. Geophys. Res.*, *113*, B06104, doi:10.1029/2007JB005502.
Chang, L., A. P. Roberts, C. J. Rowan, Y. Tang, P. Pruner, Q. Chen, and C. S. Horng (2009), Low-temperature magnetic properties of greigite (Fe_3S_4), *Geochem. Geophys. Geosyst.*, *10*, Q01Y04, doi:10.1029/2008GC002276.
Chang, L., A. P. Roberts, W. Williams, J. D. Fitz Gerald, J. C. Larrasoaña, L. Jovane, and A. R. Muxworthy (2012), Giant magnetofossils and hyperthermal events, *Earth Planet. Sci. Lett.*, *351–352*, 258–269, doi:10.1016/j.epsl.2012.07.031.
Chang, L., M. Winklhofer, A. P. Roberts, D. Heslop, F. Florindo, M. J. Dekkers, W. Krijgsman, K. Kodama, and Y. Yamamoto (2013), Low-temperature magnetic properties of pelagic carbonates: Oxidation of biogenic magnetite and identification of magnetosome chains, *J. Geophys. Res. Solid Earth*, *118*, 6049–6065, doi:10.1002/2013JB010381.
Chang, L., A. P. Roberts, M. Winklhofer, D. Heslop, M. J. Dekkers, W. Krijgsman, J. D. Fitz Gerald, and P. Smith (2014), Magnetic detection and characterization of biogenic magnetic minerals: A comparison of ferromagnetic resonance and first-order reversal curve diagrams, *J. Geophys. Res. Solid Earth*, *119*, doi:10.1002/2014JB011213.
Day, R., M. Fuller, and V. A. Schmidt (1977), Hysteresis properties of titanomagnetites: Grain size and composition dependence, *Phys. Earth Planet. Inter.*, *13*, 260–267.
Dekkers, M. J., J.-L. Mattéi, G. Fillion, and P. Rochette (1989), Grain-size dependence of the magnetic behavior of pyrrhotite during its low-temperature transition at 34 K, *Geophys. Res. Lett.*, *16*, 855–858.
Dekkers, M. J., H. F. Passier, and M. A. A. Schoonen (2000), Magnetic properties of hydrothermally synthesized greigite-II. High- and low-temperature characteristics, *Geophys. J. Int.*, *141*, 809–819.
Dong, J., S. Zhang, G. Jiang, H. Li, and R. Gao (2013), Greigite from carbonate concretions of the Ediacaran Doushantuo Formation in South China and its environmental implications, *Precambrian Res.*, *225*, 77–85.
Egli, R. (2004), Characterization of individual rock magnetic components by analysis of remanence curves, 1. Unmixing natural sediments, *Stud. Geophys. Geod.*, *48*, 391–446.
Egli, R., A. P. Chen, M. Winklhofer, K. P. Kodama, and C.-S. Horng (2010), Detection of noninteracting single domain particles using first-order reversal curve diagrams, *Geochem. Geophys. Geosyst.*, *11*, Q01Z11, doi:10.1029/2009GC002916.
Farina, M., D. M. S. Esquivel, and H. G. P. L. de Barros (1990), Magnetic iron-sulfur crystals from a magnetotactic microorganism, *Nature*, *343*, 256–258.
Frederichs, T., T. Von Dobeneck, U. Bleil, and M. J. Dekkers (2003), Towards the identification of siderite, rhodochrosite, and vivianite in sediments by their low-temperature magnetic properties, *Phys. Chem. Earth*, *28*, 669–679.
Grothe, A., F. Sangiorgi, Y. R. Mulders, I. Vasiliev, G.-J. Reichart, H. Brinkhuis, M. Stoica, and W. Krijgsman (2014), Black Sea desiccation during the Messinian Salinity Crisis: Fact or fiction?, *Geology*, *42*, 563–566.
Heslop, D., A. P. Roberts, L. Chang, M. Davies, A. Abrajevitch, and P. De Deckker (2013), Quantifying magnetite magnetofossil contributions to sedimentary magnetizations, *Earth Planet. Sci. Lett.*, *382*, 58–65.
Hesse, P. P. (1994), Evidence for bacterial palaeoecological origin of mineral magnetic cycles in oxic and sub-oxic Tasman Sea sediments, *Mar. Geol.*, *117*, 1–17.
Hounslow, M. W., and B. A. Maher (1996), Quantitative extraction and analysis of carriers of magnetization in sediments, *Geophys. J. Int.*, *124*, 57–74.
Housen, B. A., S. K. Banerjee, and B. M. Moskowitz (1996), Low-temperature magnetic properties of siderite and magnetite in marine sediments, *Geophys. Res. Lett.*, *23*, 2843–2846.
Hüsing, S. K., F. J. Hilgen, H. A. Aziz, and W. Krijgsman (2007), Completing the Neogene geological time scale between 8.5 and 12.5 Ma, *Earth Planet. Sci. Lett.*, *253*, 340–358.
Jiang, W. T., C. S. Horng, A. P. Roberts, and D. R. Peacor (2001), Contradictory magnetic polarities in sediments and variable timing of neoformation of authigenic greigite, *Earth Planet. Sci. Lett.*, *193*, 1–12.

Kao, S. J., C. S. Horng, A. P. Roberts, and K. K. Liu (2004), Carbon–sulfur–iron relationships in sedimentary rocks from southwestern Taiwan: Influence of geochemical environment on greigite and pyrrhotite formation, *Chem. Geol.*, *203*, 153–168.

Kasama, T., M. Pósfai, R. K. K. Chong, A. P. Finlayson, P. R. Buseck, R. B. Frankel, and R. E. Dunin-Borkowski (2006), Magnetic properties, microstructure, composition, and morphology of greigite nanocrystals in magnetotactic bacteria from electron holography and tomography, *Am. Mineral.*, *91*, 1216–1229.

Kirschvink, J. L., and S. B. R. Chang (1984), Ultrafine-grained magnetite in deep-sea sediments—Possible bacterial magnetofossils, *Geology*, *12*, 559–562.

Kopp, R. E., and J. L. Kirschvink (2008), The identification and biogeochemical interpretation of fossil magnetotactic bacteria, *Earth Sci. Rev.*, *86*, 42–61.

Kopp, R. E., B. P. Weiss, A. C. Maloof, H. Vali, C. Z. Nash, and J. L. Kirschvink (2006), Chains, clumps, and strings: Magnetofossil taphonomy with ferromagnetic resonance spectroscopy, *Earth Planet. Sci. Lett.*, *247*, 10–25.

Kopp, R. E., T. D. Raub, D. Schumann, H. Vali, A. V. Smirnov, and J. L. Kirschvink (2007), Magnetofossil spike during the Paleocene-Eocene thermal maximum: Ferromagnetic resonance, rock magnetic, and electron microscopy evidence from Ancora, New Jersey, United States, *Paleoceanography*, *22*, PA4103, doi:10.1029/2007PA001473.

Krijgsman, W., M. Stoica, I. Vasiliev, and V. V. Popov (2010), Rise and fall of the Paratethys Sea during the Messinian salinity crisis, *Earth Planet. Sci. Lett.*, *290*, 183–191.

Kruiver, P. P., and H. F. Passier (2001), Coercivity analysis of magnetic phases in sapropel S1 related to variations in redox conditions, including an investigation of the S ratio, *Geochem. Geophys. Geosyst.*, *2*(12), 1063, doi:10.1029/2001GC000181.

Kruiver, P. P., M. J. Dekkers, and D. Heslop (2001), Quantification of magnetic coercivity components by the analysis of acquisition curves of isothermal remanent magnetization, *Earth Planet. Sci. Lett.*, *189*, 269–276.

Langereis, C. G., W. Krijgsman, G. Muttoni, and M. Menning (2010), Magnetostratigraphy concepts, definitions, and applications, *Newsl. Stratigr.*, *43*, 207–233.

Larrasoaña, J. C., A. P. Roberts, L. Chang, S. A. Schellenberg, J. D. Fitz Gerald, R. D. Norris, and J. C. Zachos (2012), Magnetotactic bacterial response to Antarctic dust supply during the Palaeocene-Eocene thermal maximum, *Earth Planet. Sci. Lett.*, *333–334*, 122–133.

Laskar, J., P. Robutel, F. Joutel, M. Gastineau, A. C. M. Correia, and B. Levrard (2004), A long term numerical solution for the insolation quantities of the Earth, *Astron. Astrophys.*, *428*, 261–285.

Lefèvre, C. T., N. Menguy, F. Abreu, U. Lins, M. Pósfai, T. Prozorov, D. Pignol, R. B. Frankel, and D. A. Bazylinski (2011), A cultured greigite-producing magnetotactic bacterium in a novel group of sulfate-reducing bacteria, *Science*, *334*, 1720–1723.

Mann, S., N. H. C. Sparks, R. B. Frankel, D. A. Bazylinski, and H. W. Jannasch (1990), Biomineralization of ferrimagnetic greigite (Fe_3S_4) and iron pyrite (FeS_2) in a magnetotactic bacterium, *Nature*, *343*, 258–261.

Manzi, V., R. Gennari, F. Hilgen, W. Krijgsman, S. Lugli, M. Roveri, and F. J. Sierro (2013), Age refinement of the Messinian salinity crisis onset in the Mediterranean, *Terra Nova*, *25*, 315–322.

Moskowitz, B. M., R. B. Frankel, and D. A. Bazylinski (1993), Rock magnetic criteria for the detection of biogenic magnetite, *Earth Planet. Sci. Lett.*, *120*, 283–300.

Moskowitz, B. M., D. A. Bazylinski, R. Egli, R. B. Frankel, and K. J. Edwards (2008), Magnetic properties of marine magnetotactic bacteria in a seasonally stratified coastal pond (Salt Pond, MA, USA), *Geophys. J. Int.*, *174*, 75–92.

Mullender, T. A. T., A. J. van Velzen, and M. J. Dekkers (1993), Continuous drift correction and separate identification of ferrimagnetic and paramagnetic contributions in thermomagnetic runs, *Geophys. J. Int.*, *114*, 663–672.

Muxworthy, A. R., W. Williams, A. P. Roberts, M. Winklhofer, L. Chang, and M. Posfai (2013), Critical single domain grain sizes in chains of interacting greigite particles: Implications for magnetosome crystals, *Geochem. Geophys. Geosyst.*, *14*, 5430–5441, doi:10.1002/2013GC004973.

Newell, A. J. (2005), A high-precision model of first-order reversal curve (FORC) functions for single-domain ferromagnets with uniaxial anisotropy, *Geochem. Geophys. Geosyst.*, *6*, Q05010, doi:10.1029/2004GC000877.

Passier, H. F., G. J. de Lange, and M. J. Dekkers (2001), Magnetic properties and geochemistry of the active oxidation front and the youngest sapropel in the eastern Mediterranean Sea, *Geophys. J. Int.*, *145*, 604–614.

Penninga, I., H. de Waard, B. M. Moskowitz, D. A. Bazylinski, and R. B. Frankel (1995), Remanence measurements on individual magnetotactic bacteria using a pulsed magnetic field, *J. Magn. Magn. Mater.*, *149*, 279–286.

Petersen, N., T. von Dobeneck, and H. Vali (1986), Fossil bacterial magnetite in deep-sea sediments from the South Atlantic Ocean, *Nature*, *320*, 611–614.

Pike, C. R., A. P. Roberts, and K. L. Verosub (1999), Characterizing interactions in fine magnetic particle systems using first order reversal curves, *J. Appl. Phys.*, *85*, 6660–6667.

Pósfai, M., P. R. Buseck, D. A. Bazylinski, and R. B. Frankel (1998a), Reaction sequence of iron sulfide minerals in bacteria and their use as biomarkers, *Science*, *280*, 880–883.

Pósfai, M., P. R. Buseck, D. A. Bazylinski, and R. B. Frankel (1998b), Iron sulfides from magnetotactic bacteria: Structure, composition, and phase transitions, *Am. Mineral.*, *83*, 1469–1481.

Pósfai, M., K. Cziner, E. Márton, P. Márton, P. R. Buseck, R. B. Frankel, and D. A. Bazylinski (2001), Crystal-size distributions and possible biogenic origin of Fe sulfides, *Eur. J. Mineral.*, *13*, 691–703.

Radionova, E. P., and L. A. Golovina (2011), Upper Maeotian—Lower Pontian "Transitional strata" in the Taman Peninsula: Stratigraphic position and paleogeographic interpretation, *Geol. Carpathica*, *62*, 77–90.

Radionova, E. P., L. A. Golovina, N. Y. Filippova, V. M. Trubikhin, S. V. Popov, I. A. Goncharova, Y. V. Vernigorova, and T. N. Pinchuk (2012), Middle-Upper Miocene stratigraphy of the Taman Peninsula, Eastern Paratethys, *Cent. Eur. J. Geosci.*, *4*, 188–204.

Reinholdsson, M., I. Snowball, L. Zillén, C. Lenz, and D. J. Conley (2013), Magnetic enhancement of Baltic Sea sapropels by greigite magnetofossils, *Earth Planet. Sci. Lett.*, *366*, 137–150.

Reitner, J., J. Peckmann, M. Blumenberg, W. Michaelis, A. Reimer, and V. Thiel (2005), Concretionary methane-seep carbonates and associated microbial communities in Black Sea sediments, *Palaeogeogr. Palaeoclimatol. Palaeoecol.*, *227*, 18–30.

Reynolds, R. L., M. L. Tuttle, C. A. Rice, N. S. Fishman, J. A. Karachewski, and D. M. Sherman (1994), Magnetization and geochemistry of greigite-bearing Cretaceous strata, North Slope basin, Alaska, *Am. J. Sci.*, *294*, 485–528.

Roberts, A. P. (1995), Magnetic properties of sedimentary greigite (Fe_3S_4), *Earth Planet. Sci. Lett.*, *134*, 227–236.

Roberts, A. P., and R. Weaver (2005), Multiple mechanisms of remagnetization involving sedimentary greigite (Fe_3S_4), *Earth Planet. Sci. Lett.*, *231*, 263–277.

Roberts, A. P., R. L. Reynolds, K. L. Verosub, and D. P. Adam (1996), Environmental magnetic implications of greigite (Fe_3S_4) formation in a 3 million year lake sediment record from Butte Valley, Northern California, *Geophys. Res. Lett.*, *23*, 2859–2862.

Roberts, A. P., J. S. Stoner, and C. Richter (1999), Diagenetic magnetic enhancement of sapropels from the eastern Mediterranean Sea, *Mar. Geol.*, *153*, 103–116.
Roberts, A. P., C. R. Pike, and K. L. Verosub (2000), First-order reversal curve diagrams: A new tool for characterizing the magnetic properties of natural samples, *J. Geophys. Res.*, *105*, 28,461–28,475.
Roberts, A. P., Q. Liu, C. J. Rowan, L. Chang, C. Carvallo, J. Torrent, and C. S. Horng (2006), Characterization of hematite (α-Fe_2O_3), goethite (α-FeOOH), greigite (Fe_3S_4), and pyrrhotite (Fe_7S_8) using first-order reversal curve diagrams, *J. Geophys. Res.*, *111*, B12S35, doi:10.1029/2006JB004715.
Roberts, A. P., F. Florindo, J. C. Larrasoaña, M. A. O'Regan, and X. Zhao (2010), Complex polarity pattern at the former Plio–Pleistocene global stratotype section at Vrica (Italy): Remagnetization by magnetic iron sulfides, *Earth Planet. Sci. Lett.*, *292*, 98–111.
Roberts, A. P., L. Chang, C. J. Rowan, C.-S. Horng, and F. Florindo (2011a), Magnetic properties of sedimentary greigite (Fe_3S_4): An update, *Rev. Geophys.*, *49*, RG1002, doi:10.1029/2010RG000336.
Roberts, A. P., F. Florindo, G. Villa, L. Chang, L. Jovane, S. M. Bohaty, J. C. Larrasoaña, D. Heslop, and J. D. Fitz Gerald (2011b), Magnetotactic bacterial abundance in pelagic marine environments is limited by organic carbon flux and availability of dissolved iron, *Earth Planet. Sci. Lett.*, *310*, 441–452.
Roberts, A. P., L. Chang, D. Heslop, F. Florindo, and J. C. Larrasoaña (2012), Searching for single domain magnetite in the 'pseudo-single-domain' sedimentary haystack: Implications of biogenic magnetite preservation for sediment magnetism and relative paleointensity determinations, *J. Geophys. Res.*, *117*, B08104, doi:10.1029/2012JB009412.
Rochette, P., G. Fillion, J.-L. Mattéi, and M. J. Dekkers (1990), Magnetic transition at 30–34 Kelvin in pyrrhotite: insight into a widespread occurrence of this mineral rocks, *Earth Planet. Sci. Let.*, *98*, 319–328.
Roveri, M., et al. (2014), The Messinian salinity crisis: Past and future of a great challenge for marine sciences, *Mar. Geol.*, *352*, 25–58.
Rowan, C. J., and A. P. Roberts (2006), Magnetite dissolution, diachronous greigite formation, and magnetizations arising from pyrite oxidation: Unravelling complex magnetizations in Neogene marine sediments from New Zealand, *Earth Planet. Sci. Lett.*, *241*, 119–137.
Rowan, C. J., A. P. Roberts, and T. Broadbent (2009), Reductive diagenesis, magnetite dissolution, greigite growth and paleomagnetic smoothing in marine sediments: A new view, *Earth Planet. Sci. Lett.*, *277*, 223–235.
Sagnotti, L., A. Cascella, N. Ciaranfi, P. Macrì, P. Maiorano, M. Marino, and J. Taddeucci (2010), Rock magnetism and palaeomagnetism of the Montalbano Jonico section (Italy): Evidence for late diagenetic growth of greigite and implications for magnetostratigraphy, *Geophys. J. Int.*, *180*, 1049–1066.
Schumann, D., et al. (2008), Gigantism in unique biogenic magnetite at the Paleocene–Eocene Thermal Maximum, *Proc. Natl. Acad. Sci. U. S. A.*, *105*, 17,648–17,653.
Skinner, B. J., F. S. Grimaldi, and R. C. Erd (1964), Greigite, the thio-spinel of iron; a new mineral, *Am. Mineral.*, *49*, 543–555.
Simmons, S. L., S. M. Sievert, R. B. Frankel, D. A. Bazylinski, and K. J. Edwards (2004), Spatiotemporal distribution of marine magnetotactic bacteria in a seasonally stratified coastal salt pond, *Appl. Environ. Microbiol.*, *70*, 6230–6239.
Stoica, M., I. Lazar, W. Krijgsman, I. Vasiliev, D. Jipa, and A. Floroiu (2013), Palaeoenvironmental evolution of the East Carpathian foredeep during the late Miocene–early Pliocene (Dacian Basin; Romania), *Global Planet. Change*, *103*, 135–148.
Stoltz, J. F., S. B. R. Chang, and J. L. Kirschvink (1986), Magnetotactic bacteria and single-domain magnetite in hemipelagic sediments, *Nature*, *321*, 849–851.
Tric, E., C. Laj, C. Jéhanno, J.-P. Valet, C. Kissel, A. Mazaud, and S. Iaccarino (1991), High-resolution record of the Upper Olduvai transition from Po Valley (Italy) sediments: Support for dipolar transition geometry?, *Phys. Earth Planet. Inter.*, *65*, 319–336.
Van der Laan, E., S. Gaboardi, F. J. Hilgen, and L. J. Lourens (2005), Regional climate and glacial control on high-resolution oxygen isotope records from Ain el Beida (latest Miocene, northwest Morocco): A cyclostratigraphic analysis in the depth and time domain, *Paleoceanography*, *20*, PA1001, doi:10.1029/2003PA000995.
Van der Laan, E., E. Snel, E. de Kaenel, F. J. Hilgen, and W. Krijgsman (2006), No major deglaciation across the Miocene-Pliocene boundary: Integrated stratigraphy and astronomical tuning of the Loulja sections (Bou Regreg area, NW Morocco), *Paleoceanography*, *21*, PA3011, doi:10.1029/2005PA001193.
Van Velzen, A. J., M. J. Dekkers, and J. D. A. Zijderveld (1993), Magnetic iron-nickel sulfides in the Pliocene and Pleistocene marine marls from the Vrica section (Calabria, Italy), *Earth Planet. Sci. Lett.*, *115*, 43–55.
Vasiliev, I., W. Krijgsman, C. G. Langereis, C. E. Panaiotu, L. Maţenco, and G. Bertotti (2004), Towards an astrochronological framework for the eastern Paratethys Mio-Pliocene sedimentary sequences of the Focsani basin (Romania), *Earth Planet. Sci. Lett.*, *227*, 231–247.
Vasiliev, I., W. Krijgsman, M. Stoica, and C. G. Langereis (2005), Mio-Pliocene magnetostratigraphy in the southern Carpathian foredeep and Mediterranean-Paratethys correlation, *Terra Nova*, *17*, 374–387.
Vasiliev, I., M. J. Dekkers, W. Krijgsman, C. Franke, C. G. Langereis, and T. A. T. Mullender (2007), Early diagenetic greigite as a recorder of the palaeomagnetic signal in Miocene-Pliocene sedimentary rocks of the Carpathian foredeep (Romania), *Geophys. J. Int.*, *171*, 613–629.
Vasiliev, I., C. Franke, J. D. Meeldijk, M. J. Dekkers, C. G. Langereis, and W. Krijgsman (2008), Putative greigite magnetofossils from the Pliocene Epoch, *Nat. Geosci.*, *1*, 782–786.
Vasiliev, I., A. G. Iosifidi, A. N. Khramov, W. Krijgsman, K. Kuiper, C. G. Langereis, V. V. Popov, M. Stoica, V. A. Tomsha, and S. V. Yudin (2011), Magnetostratigraphy and radio-isotope dating of upper Miocene–lower Pliocene sedimentary successions of the Black Sea Basin (Taman Peninsula, Russia), *Palaeogeogr. Palaeoclimatol. Palaeoecol.*, *310*, 163–175.
Vasiliev, I., G. J. Reichart, and W. Krijgsman (2013), Impact of the Messinian salinity crisis on Black Sea hydrology—Insights from hydrogen isotopes analysis on biomarkers, *Earth Planet. Sci. Lett.*, *362*, 272–282.
Wang, Y., W. Lin, J. Li, and Y. Pan (2013), High diversity of the δ-*proteobacteria* magnetotactic bacteria in a freshwater niche, *Appl. Environ. Microbiol.*, *79*, 2813–2817.
Weiss, B. P., S. S. Kim, J. L. Kirschvink, R. E. Kopp, M. Sankaran, A. Kobayashi, and A. Komeili (2004), Ferromagnetic resonance and low temperature magnetic tests for biogenic magnetite, *Earth Planet. Sci. Lett.*, *233*, 311–324.
Wenter, R., G. Wanner, D. Schüler, and J. Overmann (2009), Ultrastructure, tactic behaviour and potential for sulfate reduction of a novel multicellular magnetotactic prokaryote from North Sea sediments, *Environ. Microbiol.*, *11*, 1493–1505.
Winklhofer, M., L. G. Abraçado, A. F. Davila, C. N. Keim, and H. G. P. L. de Barros (2007), Magnetic optimization in a multicellular magnetotactic organism, *Biophys. J.*, *92*, 661–670.
Yamazaki, T. (2012), Paleoposition of the intertropical convergence zone in the eastern Pacific inferred from glacial-interglacial changes in terrigenous and biogenic magnetic mineral fractions, *Geology*, *40*, 151–154.
Yamazaki, T., and M. Ikehara (2012), Origin of magnetic mineral concentration variation in the Southern Ocean, *Paleoceanography*, *27*, PA2206, doi:10.1029/2011PA002271.